

FINE DEFECT ENGINEERING OF GRAPHENE FRICTION

SUPPLEMENTARY DATA

Aitor Zambudio, Enrico Gnecco, Jaime Colchero, Rubén Pérez, Julio Gómez-Herrero and Cristina Gomez-Navarro

SI1. Irradiation conditions

To generate a gradient of controlled monoatomic vacancies we partially covered the sample with a stencil mask, then we irradiated the surface with Ar⁺ ions (140 eV) under high vacuum conditions. Subsequently, we shifted the mask a few microns along the long axis of the sample (X axis) and repeat the irradiation with similar conditions. Due to this shifting and together with the shadow produced by the mask, we obtained a gradient-like distribution of the defect density along the X axis, yielding an ideal sample to study friction dependence on the density of monoatomic defects.

SI2 STM images

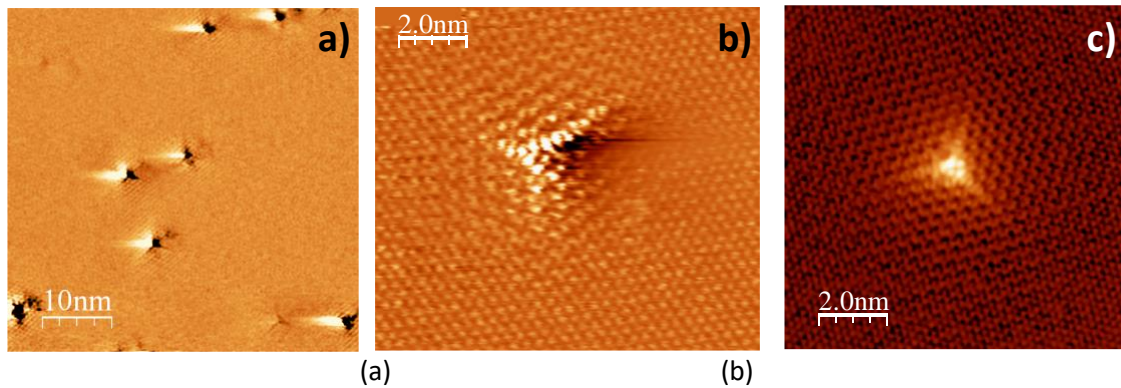


Fig. S1 – (a) STM image acquired in ambient conditions of Ar⁺ irradiated HOPG in the same conditions as our samples. The distance between vacancies measured by STM agrees with those measured by Raman spectroscopy (as shown by López-Polín *et al* [1] in SI). (b) Zoom in into a single vacancy showing the effect of monovacancies in tunnel current. These images are identical to those obtained by DFT simulations[2] and those obtained in UHV conditions, as that depicted in panel (c), courtesy of M,M. Ugeda and I. Brihuega similar to the ones published in ref [3].

SI3. Lateral Force calibration

We calibrated the electric response of the AFM photodiode (in V) into force units (in general, nN) with an original lateral force calibration method.

Firstly, the lateral spring constant of the cantilever was obtained using the normal spring constant with Colchero's approximation[4]:

$$\frac{k_{FN}}{k_{FL}} = \frac{1}{2} \left(\frac{h_{tip}}{L} \right)^2$$

Then, the lateral sensitivity of the optical beam deflection system was calculated using the normal sensitivity. The central idea behind our calibration scheme is that for a symmetric and

round reflected laser spot, the angular sensitivity of the photodiode is the same for lateral and normal directions. Applying this assumption, lateral force calibration is calculated from the normal force calibration as follows. We converted spatial F_N calibration (nm/V) to angular calibration (rad/V) using trigonometric relations and considering the cantilever bending correction factor:

$$\begin{cases} \tan\beta \approx \beta = \frac{3\Delta z}{2L} \\ \alpha = 2\beta \end{cases} \quad \text{Bending correction factor}$$

$$p_{F_N}^{-1} \left(\frac{\text{rad}}{\text{V}} \right) = \frac{\alpha}{\Delta F_N} = \frac{3}{\Delta F_N} \frac{\Delta z}{L} = \frac{3}{L} p_{F_N}^{-1} \left(\frac{\text{nm}}{\text{V}} \right)$$

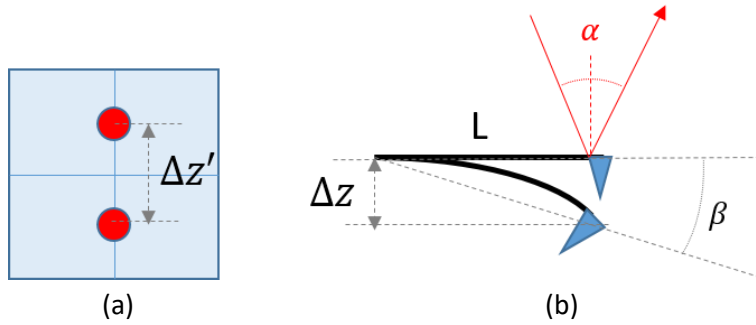


Fig. S2 – (a) Photodiode scheme showing laser beam for different cantilever bendings. (b) Scheme depicting normal bending of cantilever together with involved angles and distances. Where α is the laser beam deviation angle and β the bending angle of the cantilever edge (fig. S3). Assuming our gaussian laser beam as circular shaped, angular sensitivity of photodiode is equal in normal and lateral torsion:

$$p_{F_N}^{-1} \left(\frac{\text{rad}}{\text{V}} \right) = p_{F_L}^{-1} \left(\frac{\text{rad}}{\text{V}} \right)$$

Then we converted back to linear calibration, using the geometry of the tip:

$$\begin{cases} \tan\beta \approx \beta = \frac{\Delta x}{h_{tip}} \\ \alpha = 2\beta \end{cases} \quad p_{F_L}^{-1} \left(\frac{\text{rad}}{\text{V}} \right) = \frac{\alpha}{\Delta F_L}$$

$$p_{F_L}^{-1} \left(\frac{\text{nm}}{\text{V}} \right) = \frac{\Delta x}{\Delta F_L} = \frac{h_{tip} \alpha / 2}{\Delta F_L} = \frac{h_{tip}}{2} p_{F_L}^{-1} \left(\frac{\text{rad}}{\text{V}} \right)$$

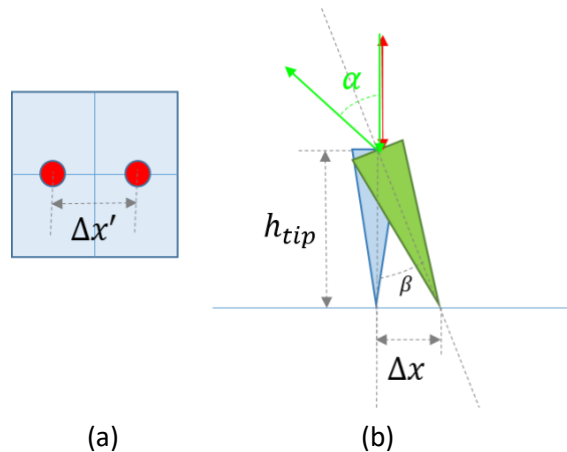


Fig. S3 – (a) Photodiode scheme showing laser beam for different lateral torsions of the cantilever. (b) Scheme illustrating lateral torsion of the tip.

And finally, to convert to lateral force units (nN), we use the above mentioned lateral spring constant: $F_L(nN) = F_L(V) \times k_{F_L} \left(\frac{nN}{nm} \right) \times p_{F_L}^{-1} \left(\frac{nm}{V} \right)$

If we summarize all the steps in a single equation, we finally obtain the following expression for F_L calibration in force units:

$$F_L(nN) = F_L(V) \times 3 \frac{L}{h_{tip}} \times k_{F_N} \left(\frac{nN}{nm} \right) \times p_{F_N}^{-1} \left(\frac{nm}{V} \right)$$

Our F_L calibration method has some important advantages over other *in situ* experimental methods:

- Time-related calibration – Almost simultaneous calibration to image acquisition.
- Error reduction – Measurement errors are minimized since we use few and well-defined parameters, which have a good signal/noise ratio.
- Non-invasive method.

SI4. Prandtl-Tomlinson Simulations

The numeric simulations have been run assuming that a point mass $m = 5 \times 10^{-11}$ kg representing the tip apex is driven elastically by a support moving with a constant velocity $v_{scan} = 25$ nm/s forth and back on a distance of 5 nm along the x axis and then upwards by $\Delta y = 16.7$ pm and so on for 300 times. The spring constant is $k = 5$ N/m. The interaction of the tip with the graphene sample including an atomic vacancy is described by a hexagonal potential with a Gaussian potential well:

$$U(x, y) = -\frac{U_G}{2} \left(2 \cos \frac{2\pi x}{a} \cos \frac{2\pi y}{a\sqrt{3}} + \cos \frac{4\pi y}{a\sqrt{3}} \right) - U_1 \exp \left(-\frac{x^2 + (y - a/\sqrt{3})^2}{2\sigma^2} \right) \quad (1)$$

In eq. (1) $a = 0.246$ nm is the lattice constant of graphene, $U_G = 0.4$ eV, $U_1 = 3$ eV, $\sigma = a/6$. Note that the center of the Gaussian is slightly above the origin to have it at the location of a missing atom, see Fig. S6. An additional viscous force $\mathbf{f} = -\gamma m \mathbf{v}$ with $\gamma = 10\gamma_c$, where $\gamma_c = 2(k/m)^{1/2}$ is the critical damping of the free oscillator, guarantees that the point mass quickly sticks to the closest minimum defined by the potential in eq. (1) after slip. \mathbf{v} is the velocity of the tip apex (different from the scan velocity). Thermal noise is introduced by adding a noise term $\xi(t)$ satisfying the fluctuation-dissipation theorem,

$$\langle \xi(t) \xi(t') \rangle = 2m\gamma k_B T \delta(t - t'), \quad (2)$$

to the equations of motion of the point mass:

$$m \frac{d^2 x}{dt^2} + m\gamma \frac{dx}{dt} + \frac{\partial U_{tot}}{\partial x} = \xi(t) \quad (3)$$

and similar for the y coordinate. In eq. (3) U_{tot} is the sum of the interaction potential U defined by eq. (1) and the (time-dependent) elastic potential

$$U_{el} = \frac{1}{2} k (\mathbf{r}_{sup} - \mathbf{r})^2 \quad (4)$$

where \mathbf{r}_{sup} and $\mathbf{r} \equiv (x, y)$ are the support position and tip position respectively. The last one is finally used to determine the longitudinal component of the spring force F_x , which is

mapped as a function of the support position on the xy plane giving the result in Fig. 2(c) in the main manuscript.

We noted that the starting points of the stick phases originated by the potential well in the forward and backward scans coincide in the simulations, whereas they are separated by about 1 nm in the experiments (as seen in the cross-section of the friction maps in Fig. 2e and 2f. This effect can be attributed to the finite size of the contact formed by tip and surface, as already noticed in other works and could be in principle reproduced by atomistic simulations with a proper arrangement of atoms at the tip apex,[5] which go beyond the goals of the present work.

S15 Friction Analysis

In order to clarify the difference between lateral force and friction force, we consider the following definitions:

- **Lateral Force:** Force experienced by the tip due to lateral displacement over the sample, pointing to the opposite direction of scan. As detailed above, this force is measured at every xy position on the sample by the AFM photodiode due to laser bending generated by the cantilever torsion. We note that, experimentally, the F_L have in general a significant offset.
- **Friction Force:** Half of the difference between averaged lateral force in forward and backward scan (“friction loop”) along a line or an image. Friction force is a measure of the average force in a closed lateral force cycle.

$$F_{Friction} = \frac{F_{Lateral,Forward} - F_{Lateral,Backward}}{2}$$

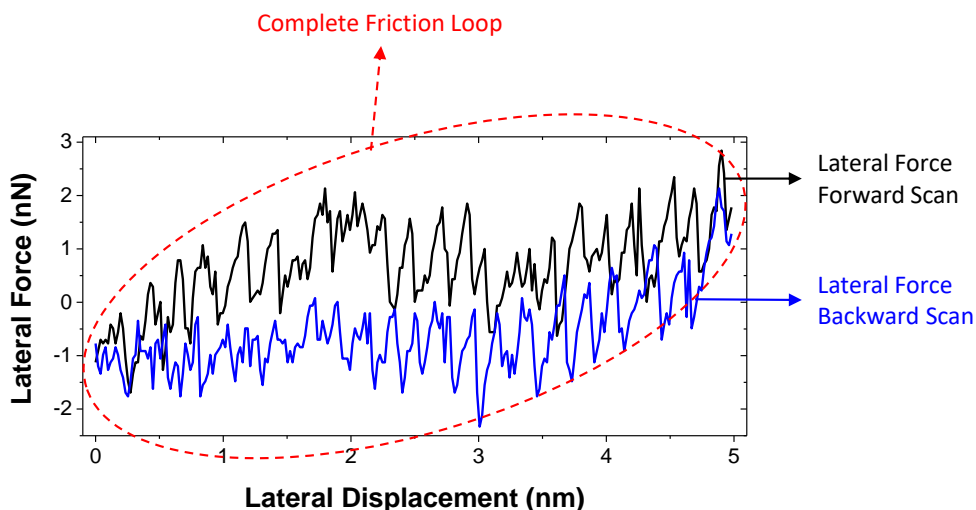


Fig. S5 – Friction loop on a pristine graphene sample, showing stick-slip pattern along forward and backward scan directions.

Friction images acquired on irradiated graphene exposed 3 types of regions with different friction behaviour:

1. A very sharp and highly increased friction very localized at defects sites.
2. An altered region surrounding the defect with a lower enhancement of friction.
3. And the remaining unaltered graphene zones, with very low friction, comparable to pristine graphene.

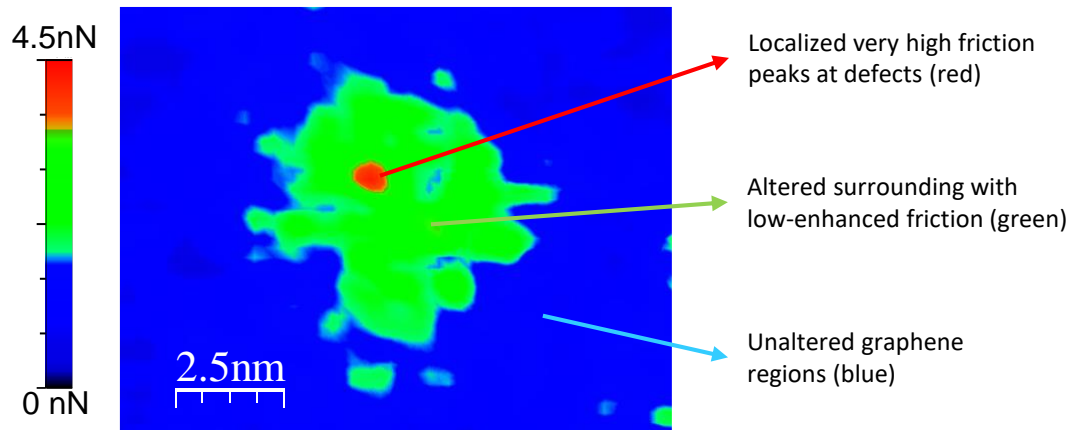


Fig. S6 – Illustrative lateral force image showing the 3 types of regions observed on irradiated samples: Localized very high friction peaks at defects (red); the altered region surrounding the defect (green), with low-enhanced friction; and the remaining unaltered graphene regions (blue)

Thanks to a homemade algorithm we were able to extract the friction coefficient (μ_{eff}) of the very localized high friction peaks at defects ($\sim 1\text{nm}^2$), and then to analyse and quantify its influence on the global friction, and compare it with the remaining graphene regions (altered low enhanced friction, and unaltered regions), surrounding this defects.

This analysis is performed using Mathematica software. Defects are localized from AFM movies (consecutives AFM friction images varying applied normal force) using a weight function which considers the height and the curvature of every friction point and extracts the values to calculate friction properties. Once we have localized the defects, we are able to study the remaining regions as well.

From this thorough analysis, we obtain a nearly constant effective friction coefficient for the localized friction peaks at defect of 0.23.

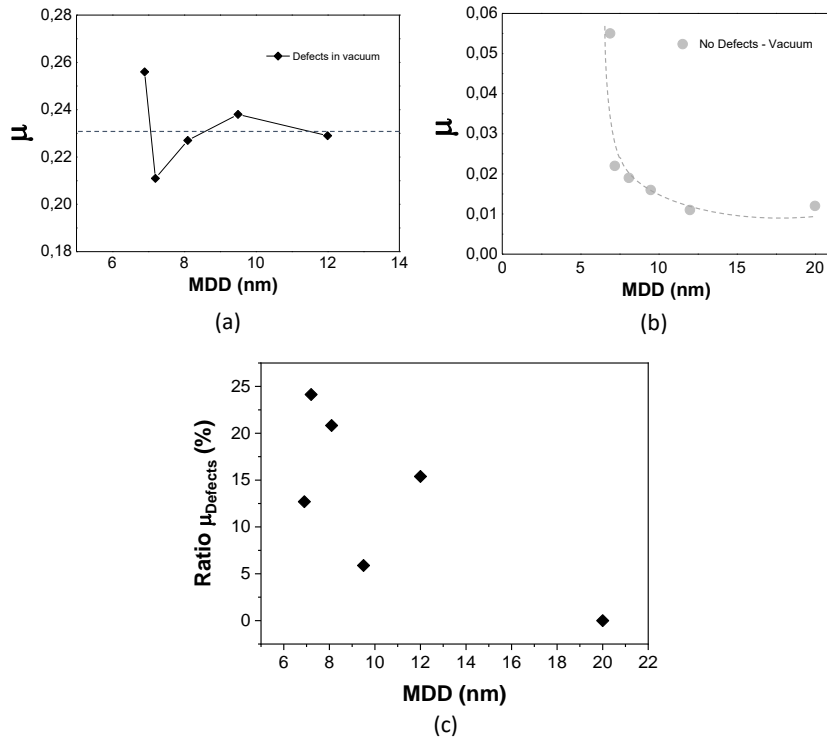


Fig. S7 – (a) Friction coefficient (μ_{eff}) extracted from the algorithm corresponding to the regions of very localized friction peaks at defects, with a nearly constant value of $\mu_{\text{defects}} \cong 0.23$. (b) Friction coefficient corresponding to the remaining (altered and unaltered) zones. We observe a clear enhancement of $\mu_{\text{no-defects}}$ with increasing defect density. (c) Ratio between friction coefficient at high friction peaks and global friction coefficient.

References

- [1] G. López-Polín, C. Gómez-Navarro, V. Parente, F. Guinea, M.I. Katsnelson, F. Pérez-Murano, J. Gómez-Herrero, Increasing the elastic modulus of graphene by controlled defect creation, *Nature Phys.* 11 (2015) 26–31. <https://doi.org/10.1038/nphys3183>.
- [2] H.A. Mizes, J.S. Foster, Long-Range Electronic Perturbations Caused by Defects Using Scanning Tunneling Microscopy, *Science*. 244 (1989) 559–562. <https://doi.org/10.1126/science.244.4904.559>.
- [3] M.M. Ugeda, I. Brihuega, F. Guinea, J.M. Gómez-Rodríguez, Missing Atom as a Source of Carbon Magnetism, *Phys. Rev. Lett.* 104 (2010) 096804. <https://doi.org/10.1103/PhysRevLett.104.096804>.
- [4] J. Colchero, *Reibungsmikroskopie (Friction Microscopy)*, Konstanz University, 1993.
- [5] U. Wyder, A. Baratoff, E. Meyer, L.N. Kantorovich, J. David, S. Maier, T. Filleter, R. Bennewitz, Interpretation of atomic friction experiments based on atomistic simulations, *J. Vac. Sci. Technol. B*. 25 (2007) 1547. <https://doi.org/10.1116/1.2770743>.
- [6] O.E. Dagdeviren, Exploring load, velocity, and surface disorder dependence of friction with one-dimensional and two-dimensional models, *Nanotechnology*. 29 (2018) 315704. <https://doi.org/10.1088/1361-6528/aac43b>.